

# Tandem internal electric fields in intralayer/interlayer carbon nitride homojunction with a directed flow of photo-excited electrons for photocatalysis



Jinqiang Zhang<sup>a</sup>, Xiaojie Tan<sup>b</sup>, Lei Shi<sup>c</sup>, Haijun Chen<sup>d,\*</sup>, Yazi Liu<sup>e</sup>, Shuaijun Wang<sup>f</sup>, Xiaoguang Duan<sup>a</sup>, Mingbo Wu<sup>b</sup>, Hongqi Sun<sup>f,\*</sup>, Shaobin Wang<sup>a,\*</sup>

<sup>a</sup> School of Chemical Engineering, The University of Adelaide, North Terrace, Adelaide, SA 5005, Australia

<sup>b</sup> State Key Laboratory of Heavy Oil Processing, Institute of New Energy, College of Chemical Engineering, China University of Petroleum (East China), Qingdao 266580, China

<sup>c</sup> College of Materials Science and Engineering, Nanjing Forestry University, Nanjing 210037, China

<sup>d</sup> Jiangsu Key laboratory of Process Enhancement and New Energy Equipment Technology, School of Mechanical and Power Engineering, Nanjing Tech University, Nanjing 211816, Jiangsu, China

<sup>e</sup> School of Environment, Nanjing Normal University, Jiangsu Engineering Lab of Water and Soil Eco-Remediation, Nanjing 210023, China

<sup>f</sup> School of Science, Edith Cowan University, 270 Joondalup Drive, Joondalup, WA 6027, Australia

## ARTICLE INFO

### Keywords:

Integrated carbon nitride homojunction  
Tandem internal electrical field  
Directed charge flow  
Maximum photocatalysis  
Hydrogen production

## ABSTRACT

Photocatalytic hydrogen production is a green technology while significantly impeded by the sluggish and uncontrolled charge dynamics for less electron accumulation on catalyst surface. Herein, we proposed an effective strategy of epitaxial growth of a van der Waals (VDW) homojunction on an intralayer homojunction of carbon nitride for a controlled charge flow. Experimental and simulation collectively disclosed a tandem internal electric field (IEF) in the integrated hybrid, stringing a lateral IEF along the intralayer homojunction with a vertical IEF within the VDW homojunction. The planar IEF dominates laterally dispersive movement of charge carriers for their efficient separations and mobilities, meanwhile the vertical IEF induces an oriented accumulation of the dispersive hot electrons to the catalyst surface for intensified hydrogen reduction. The tandem IEF renders the hydrogen evolution rate at 3.5-fold higher than in-planar homojunction, and 6.3 times higher than g-C<sub>3</sub>N<sub>4</sub> benchmark. This work realizes charge-directing dynamics for robust photocatalysis.

## 1. Introduction

Photocatalytic water splitting reaction has demonstrated its high feasibility to generate green hydrogen without carbon emissions [1,2]. Considering the highest energy density by weight, industrialization of green hydrogen production will significantly tackle the challenges in global energy crisis and environmental deterioration, thereby achieving the goal of carbon neutrality [3,4]. Cheap photocatalysts with high visible light harvesting and robust reduction capabilities are highly desired to realize the scaling production of green hydrogen [4–6]. Polymeric carbon nitride is a prevailing metal-free photocatalyst in water splitting reaction. The superiorities of visible light response, easy to be synthesized and stable in a wide pH range render carbon nitride based photocatalysts appealing in photocatalytic water splitting in the past decade. Nevertheless, the light harvesting efficiency and

photocatalytic throughputs of state-of-the-art carbon nitride photocatalysts are still far from meeting the requirements for practical applications [7–12].

Photocatalytic hydrogen production is a chain process involving the generation of hot electrons and their effective and directional outputs on catalyst surface for hydrogen reduction [13]. There are two resistances in carbon nitride toward impeding charge movements: one is the strong Coulomb force within a plane, and the other is the high energy barrier between interlayer stacking [14–19]. The former resistance always leads to a fast charge recombination, while the latter results in an easy dissipation or cooling of hot carriers during their transportation. While multifarious modification strategies, including a new concept of volume photocatalysis, have been proposed to improve the photocatalytic efficiency [20,21], the dynamics of photo-excited charge carriers in carbon nitride, including their separations, migrations and outputs, intrinsically

\* Corresponding authors.

E-mail addresses: chenjh@njtech.edu.cn (H. Chen), h.sun@ecu.edu.au (H. Sun), shaobin.wang@adelaide.edu.au (S. Wang).

determining the photocatalytic activities, remain sluggish and orderless due to the insufficient intralayer and interlayer driving forces in the catalyst.

An internal electric field (IEF) of a semiconductor based photocatalyst is a backstage manipulator to pose inherent driving forces on charge carriers and determines their dynamics and behaviors after excitations [22–26]. Its effect is becoming more prominent and has been recently brought to the forefront of photocatalysis. Unfortunately, IEFs are negligible in pristine carbon nitride due to the laterally symmetric unit cells and vertically periodic interlayer stacking, which reduce separation rate of charge carriers and their assembling on catalyst surface [27]. Fabrication of intralayer heterojunctions is an effective route to break the lateral symmetry of carbon nitride. For instance, doping with heteroatoms or creation of vacancy can enlarge the IEF along carbon nitride in plane for an enhanced photocatalysis. Besides, considerable works have been reported on fabrication of interlayer heterojunctions, including oriented heterojunction, to pose vertical IEFs on electron-hole pairs to accelerate their separations at the intimate contact [24,28–31]. However, subsequent accumulation of hot electrons on catalyst surface is of equal importance to the fast separation of charge carriers for photocatalytic hydrogen reduction, which has been overlooked.

Herein, we developed a three-dimensional carbon nitride homojunction (tandem-C<sub>3</sub>N<sub>4</sub>) by the integration of a carbon nitride van der Waals (VDW) homojunction on an carbon nitride intralayer homojunction (intra-C<sub>3</sub>N<sub>4</sub>). Characterizations disclosed that the shallow layers of tandem-C<sub>3</sub>N<sub>4</sub> are carbon doped intra-C<sub>3</sub>N<sub>4</sub>, while the bulk remains as intra-C<sub>3</sub>N<sub>4</sub>, thus both the intralayer and interlayer symmetries of carbon nitride are broken. Experimental and computation simulation collaboratively revealed a tandem IEF comprising of a lateral and a vertical IEF in tandem-C<sub>3</sub>N<sub>4</sub>. Lateral IEF dominated the rapidly planar separation and movement of charge carriers, while the extra longitudinal IEF essentially directs the accumulation of more hot electrons on the catalyst surface, accomplishing a three-dimensional modulation of charge dynamics in a directed way. Accompanied with the short vertical diffusion pathway of hot electrons within the shallow layers of the VDW carbon nitride homojunction, a much higher photocatalytic hydrogen production was achieved, exhibiting 3.5-fold higher than in-planar homojunction and 6.3 times higher than g-C<sub>3</sub>N<sub>4</sub>.

## 2. Experimental section

### 2.1. Catalyst preparation

For fabrication of an intralayer carbon nitride homojunction with a lateral IEF, 5 g of melamine and 0.5 g of sodium nitrate were fully dissolved and mixed in ultrapure water. Then, the solution was dried at 100 °C and the obtained powder was placed in a vacuum oven (60 °C) overnight. After that, the precursor was ground and put into a muffle furnace. A heat treatment of the precursor was performed at 550 °C for 4 h with a ramping rate of 2.3 °C min<sup>-1</sup>. After cooling down to room temperature, the powder was successively washed by hot water and ethanol for several times and subsequently dried at 60 °C overnight to obtain a final product (named as intra-C<sub>3</sub>N<sub>4</sub>). For comparison, pristine g-C<sub>3</sub>N<sub>4</sub> was prepared similarly without the addition of sodium nitrate.

Integrated carbon nitride homojunction with tandem lateral and vertical IEFs was synthesized by an epitaxial growth method in a self-designed furnace. The obtained intra-C<sub>3</sub>N<sub>4</sub> sample was placed in a sample holder where methane gas can go through the catalyst bed. Then, the furnace was successively purged with Ar and a mixture gas of CH<sub>4</sub> and Ar (a ratio of 1:1 and flow rate of 10 mL/min). The furnace was heated up to 500 °C for 2 h at a ramping rate of 2.3 °C min<sup>-1</sup>. The obtained product was named as tandem-C<sub>3</sub>N<sub>4</sub>.

### 2.2. Characterizations

The crystal structures of the prepared samples were analyzed by X-ray diffraction (XRD, X'Pert PRO MPD, Holland). A Micromeritics Tristar 3000 was employed to obtain N<sub>2</sub> adsorption-desorption isotherms under – 196 °C. A Talos F200X and a Hitachi SU8010 were used to capture transmission electron microscopy (TEM, and high resolution TEM, HRTEM) and scanning electron microscopy (SEM) images, respectively. A Bruker ADVANCEIII 500 MHz equipment was employed to collect solid-state <sup>13</sup>C NMR spectra. Fourier transform infrared (FT-IR) spectra were recorded on a Nicolet Nexus 670 spectrometer. Diffused reflectance spectra and photoluminescence spectra were collected on a TU-1901 spectrometer with BaSO<sub>4</sub> as a reflectance standard and a Hitachi F-4600 luminescence spectrophotometer, respectively. Time-resolved decay spectra were acquired on a FLS1000. A Kratos Axis Ultra DLD system under ultrahigh vacuum condition was used for X-ray photo-electron spectroscopy (XPS), and the results were calibrated with C 1 s reference signal (284.6 eV). A Bruker EMS-plus instrument was adopted to record solid electron paramagnetic resonance (EPR) results, which were analyzed with a Bruker Xeon software. An CEL-SPS1000 (Beijing China Education AuLight Co. Ltd., China) was used to perform surface photovoltage spectroscopy (SPV) measurements. Z potential was determined using a Malvern Zetasizer Nano ZS90 and the dispersion solution was adjusted to a pH of 7, which closely mimics the environment of the catalysts in a photocatalytic water splitting reaction.

### 2.3. Performance evaluation

Photocatalytic water splitting for H<sub>2</sub> was performed in a LabSolar-III AG reaction cell (Beijing PerfectLight Co.) equipped with a 300 W Xe-lamp (CEL-HXF300, Beijing Cel Sci-tech Co., Ltd.). A visible-light long-pass filter was used as the visible light source. In the reaction, 50 mg photocatalyst was put in 50 mL aqueous solution with 0.8 mL of H<sub>2</sub>PtCl<sub>6</sub>·(H<sub>2</sub>O)<sub>6</sub> (3.0 wt%), and 5 mL of triethanolamine. Prior to light irradiation, the reactor was evacuated for 30 min to thoroughly remove air inside. The reaction temperature was kept at 6 °C. H<sub>2</sub> was finally determined by an online gas chromatograph (GC7920, Techcomp) equipped with a 5 Å molecular sieve column and a thermal conduction detector (TCD).

### 2.4. Electrochemical measurements

The electrochemical measurements of the prepared samples were performed on a CHI 760E electrochemical workstation (CH Instruments, Shanghai, China) with a three-electrode framework including a working electrode, an Ag/AgCl reference electrode, and a platinum counter electrode. The working electrodes were prepared using Indium Tin Oxide (ITO) glasses decorated with the prepared samples. Specifically, a slurry was prepared by mixing photocatalyst (10 mg) with 20 μL Nafion in 1 mL of ethanol solution, and then was dispersed onto the ITO (2 cm × 5 cm). After naturally dried, the electrode was put into an oven at 80 °C for 2 h. Na<sub>2</sub>SO<sub>4</sub> solution (0.1 M) was used as the electrolyte. A 300 W Xenon lamp was used as the visible light source. For the tests of electrochemical impedance spectroscopy (EIS), the frequency ranged from 100 kHz to 10 mHz with the perturbation signal of 10 mV.

### 2.5. Computational methods

First-principles density functional theory (DFT) calculations were performed using Vienna Ab initio Simulation Package (VASP) with the projector augmented wave (PAW) method. The exchange-functional was treated by the generalized gradient approximation (GGA) of Perdew-Burke-Ernzerhof (PBE) functional. HSE06 hybrid functional was used for more accurate calculations of electronic structure. The energy cutoff was set at 500 eV for the plane wave basis expansion and the force on each atom was set less than 0.02 eV/Å for convergence criterion of

geometry relaxation. The Monkhorst-Pack K-mesh was applied for the Brillouin-zone integration in the calculation, with the K-point separation of  $0.04 \text{ \AA}^{-1}$ . A convergence energy threshold of  $10^{-5} \text{ eV}$  was set in the self-consistent calculations.

### 3. Results and discussion

The processes to integrate tandem-C<sub>3</sub>N<sub>4</sub> are shown in Fig. 1a. Pristine carbon nitride (g-C<sub>3</sub>N<sub>4</sub>) with centrosymmetric and periodical tri-s-triazine rings was synthesized by direct calcination of melamine at 550 °C (left model in Fig. 1a). To break up the lateral symmetry, we added NaNO<sub>3</sub> salt during the polymerization of carbon nitride to make

damage to the triazine ring, acquiring a intralayer homojunction (intra-C<sub>3</sub>N<sub>4</sub>, middle model in Fig. 1a). Then an extra longitudinal VDW homojunction was created on intra-C<sub>3</sub>N<sub>4</sub> by further calcination under methane atmosphere. The carbon radicals from methane pyrolysis replaced nitrogen atoms on the shallow layers of intra-C<sub>3</sub>N<sub>4</sub> to further break up the longitudinal symmetry. As the bulk structure of intra-C<sub>3</sub>N<sub>4</sub> homojunction maintained, a tandem carbon nitride homojunction (tandem-C<sub>3</sub>N<sub>4</sub>, right model in Fig. 1a) was obtained, which was comprised of a lateral carbon nitride intralayer homojunction and a vertical carbon nitride VDW homojunction.

XRD patterns were collected to study the crystalline structure of the different types of carbon nitride homojunctions (Fig. 1b). Two obvious

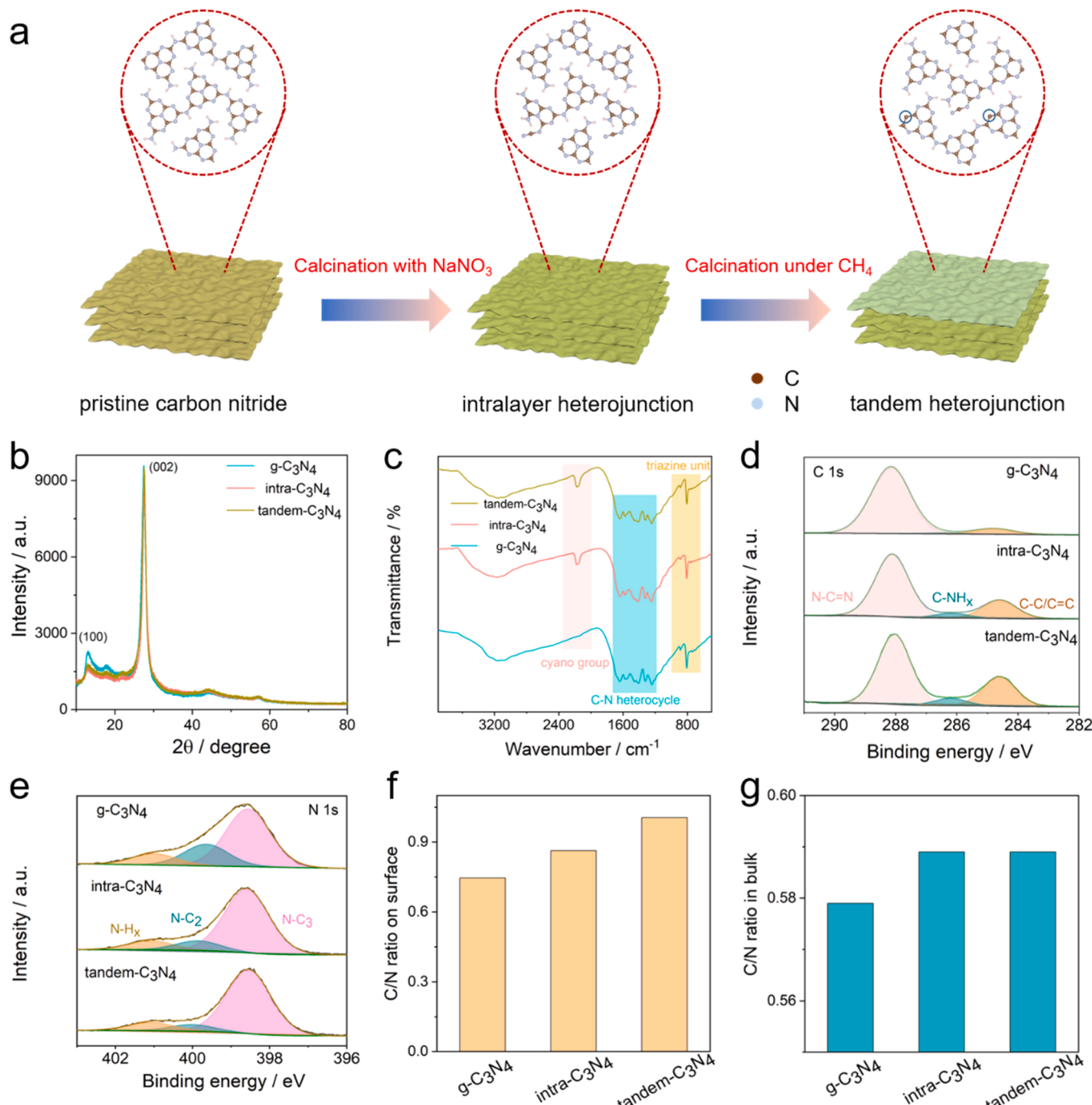


**Fig. 1.** Catalyst synthesis and characterizations. (a) Schematic illustration for integration of intralayer and VDW homojunctions in a tandem carbon nitride homojunction. Compositional information of g-C<sub>3</sub>N<sub>4</sub>, intra-C<sub>3</sub>N<sub>4</sub> and tandem-C<sub>3</sub>N<sub>4</sub>, including (b) XRD patterns, (c) FT-IR spectra, high resolution XPS C 1 s (d) and N 1 s (e) spectra, (f) C/N ratio on surface determined by XPS tests and (g) C/N ratio in bulk revealed from element analysis (EA).

characteristic peaks at 13.0 and 27.4° can be observed on pristine carbon nitride. The former peak is ascribed to the (100) diffraction of laterally periodic tri-s-triazine units, while the latter one is attributed to the (002) vertical stacking diffraction of the graphitic structure [32–34]. Compared with pristine g-C<sub>3</sub>N<sub>4</sub>, the intensity for the (100) peak of intra-C<sub>3</sub>N<sub>4</sub> and tandem-C<sub>3</sub>N<sub>4</sub> apparently decreased but the (002) peak kept unchanged. This means that the planar triazine structure of g-C<sub>3</sub>N<sub>4</sub> was destroyed after calcination of melamine with NaNO<sub>3</sub> and the damaged triazine structure failed to be recovered after further calcination of intra-C<sub>3</sub>N<sub>4</sub> under methane [6]. Meanwhile, neither NaNO<sub>3</sub> nor methane failed to break the interlayer van der Waals interaction of g-C<sub>3</sub>N<sub>4</sub> during the calcination. This is consistent with the observations of the unchanged bulk morphology of intra-C<sub>3</sub>N<sub>4</sub> and tandem-C<sub>3</sub>N<sub>4</sub> from TEM images (Fig. S1). As such, the symmetric and periodical unit cells within the intralayer structure of g-C<sub>3</sub>N<sub>4</sub> were destroyed in intra-C<sub>3</sub>N<sub>4</sub> and tandem-C<sub>3</sub>N<sub>4</sub>, but their thickness of cross section remained.

Fourier transform infrared (FT-IR) spectroscopy was then employed to investigate the molecular structure of intra-C<sub>3</sub>N<sub>4</sub> and tandem-C<sub>3</sub>N<sub>4</sub> (Fig. 1c). Absorption bands at 810, 1200–1750 and 3000–3700 cm<sup>-1</sup> can be clearly seen in all the three samples, which are corresponded to the breathing mode of triazine units, stretching mode of N-containing heterocycles, and the N-H stretch of marginal amino groups, respectively, indicating the main C-N frameworks maintain (unit cell of C<sub>3</sub>N<sub>4</sub>, Fig. S2a) after the fabrication of lateral and vertical homojunctions [35]. The result is also supported by the two evident <sup>13</sup>C NMR peaks of C=N carbon atoms at 165 ppm and C-NH<sub>2</sub> carbon atom at 155 ppm in intra-C<sub>3</sub>N<sub>4</sub> and tandem-C<sub>3</sub>N<sub>4</sub> samples (Fig. S3) [36]. Noticeably, an obvious peak emerged at 2170 cm<sup>-1</sup> on intra-C<sub>3</sub>N<sub>4</sub> (Fig. 1c), which is assigned to the asymmetric stretching vibration of cyano groups [37]. The intriguing result suggested that the triazine ring in the carbon nitride framework was opened after calcination with sodium salt, leaving nitrogen vacancies in the unit cell (unit cell of N<sub>v</sub>-C<sub>3</sub>N<sub>4</sub>, Fig. S2b). It should be noted that further calcination of intra-C<sub>3</sub>N<sub>4</sub> under methane failed to recover the melem structure. This well matched with the similar (100) peak between intra-C<sub>3</sub>N<sub>4</sub> and tandem-C<sub>3</sub>N<sub>4</sub> in their XRD profiles, confirming that the intralayer homojunction exists in both the samples.

We then use X-ray photoelectron spectroscopy (XPS) to study the surface composition of the as-prepared samples (Fig. S4 and Table S1). C1s spectra are deconvoluted into three peaks at around 284.6, 285.7 and 288.1 eV, which are assigned to the C=C bonding, sp<sup>2</sup>-hybridized C bonded to the amino group (C-NH<sub>2</sub>), and sp<sup>2</sup>-hybridized C bonded to N inside the triazine rings (N-C≡N), respectively (Fig. 1d) [33]. Compared with g-C<sub>3</sub>N<sub>4</sub>, the C-NH<sub>2</sub> peak of intra-C<sub>3</sub>N<sub>4</sub> at 286.0 eV was intensified and upshifted. As the binding energy of cyano group is similar to amino group, the intensified and upshifted peak at 286.0 eV proves the creation of the cyano group in intra-C<sub>3</sub>N<sub>4</sub> sample, indicating the damage of triazine rings [37].

N 1 s spectra are fitted to the peaks at 398.6, 399.7 and 400.9 eV, which are attributed to the tertiary N (N-(C)<sub>3</sub>), sp<sup>2</sup>-hybridized N (C-N=C), and amino group (-N-H), respectively (Fig. 1e) [38]. Compared with g-C<sub>3</sub>N<sub>4</sub>, the N-C<sub>2</sub> peak on intra-C<sub>3</sub>N<sub>4</sub> was obviously upshifted and weakened (Table S2). This again proves the damaged triazine structure when calcination of melamine with NaNO<sub>3</sub>. A further upshift and decrease of N-C<sub>2</sub> peak can be observed after calcination under methane gas, suggesting that some N atoms were replaced by the carbon atoms from decomposed methane molecules to form C=C bonding. Meanwhile, D and G bands assigning to defect carbon and graphitic carbon, respectively, fail to be found on tandem-C<sub>3</sub>N<sub>4</sub> from Raman spectra (Fig. S5), indicating that C-doped carbon nitride intralayer homojunction (unit cell of C-N<sub>v</sub>-C<sub>3</sub>N<sub>4</sub>, Fig. S2c), rather than carbon material was formed in tandem-C<sub>3</sub>N<sub>4</sub>.

We further compared the element contents in the bulk structure of the three samples (determined by element analysis) with those on catalyst surface (revealed from XPS) [39]. As displayed in Fig. 1f-g and Table S3-4, the C/N ratio of g-C<sub>3</sub>N<sub>4</sub> surface within shallow layers

gradually increased after NaNO<sub>3</sub> and subsequent methane treatments. The overall C/N ratio of intra-C<sub>3</sub>N<sub>4</sub> measured by element analysis also increased compared with g-C<sub>3</sub>N<sub>4</sub>, illustrating that the nitrogen vacancies were created throughout the whole structure of intra-C<sub>3</sub>N<sub>4</sub>. While the bulk carbon content after calcination under methane is almost the same as intra-C<sub>3</sub>N<sub>4</sub>. The results indicate that substitution of nitrogen by carbon atom occurs only on the top layers of intra-C<sub>3</sub>N<sub>4</sub>, thereby forming an extra carbon nitride van der Waals homojunction in tandem-C<sub>3</sub>N<sub>4</sub>. Therefore, an intralayer homojunction exists in intra-C<sub>3</sub>N<sub>4</sub>, and an additional van der Waals homojunction is formed in tandem-C<sub>3</sub>N<sub>4</sub>.

The IEFs in the different types of carbon nitride homojunctions were theoretically studied. Single layer models of C<sub>3</sub>N<sub>4</sub>, N<sub>v</sub>-C<sub>3</sub>N<sub>4</sub> and C-N<sub>v</sub>-C<sub>3</sub>N<sub>4</sub> were built to represent the different components in intralayer and VDW carbon nitride homojunctions (Fig. S2). The bandgaps for C<sub>3</sub>N<sub>4</sub>, N<sub>v</sub>-C<sub>3</sub>N<sub>4</sub> and C-N<sub>v</sub>-C<sub>3</sub>N<sub>4</sub> were calculated to be 3.65, 3.17 and 2.52 eV, respectively (Fig. 2a), suggesting that the creation of nitrogen vacancy and carbon doping are both effective pathways to improve the light absorption. Combined with the calculated conduction (CB) and valence bands (VB), the band structures of these three models are presented in Fig. 2b. Meanwhile, the work functions for the three models were acquired (Fig. 2c-e). In the intra-C<sub>3</sub>N<sub>4</sub>, the work functions for C<sub>3</sub>N<sub>4</sub> and N<sub>v</sub>-C<sub>3</sub>N<sub>4</sub> unit cells were estimated to be 6.57 and 6.45 eV, respectively. As thus, when N<sub>v</sub>-C<sub>3</sub>N<sub>4</sub> and C<sub>3</sub>N<sub>4</sub> unit cells are laterally combined, the electrons will flow from N<sub>v</sub>-C<sub>3</sub>N<sub>4</sub> to C<sub>3</sub>N<sub>4</sub> unit cells until their Fermi levels are equilibrated, leaving positive charges on C<sub>3</sub>N<sub>4</sub> unit cells. Consequently, an internal electric field would be created in intra-C<sub>3</sub>N<sub>4</sub>, horizontally directing from C<sub>3</sub>N<sub>4</sub> to N<sub>v</sub>-C<sub>3</sub>N<sub>4</sub> (Fig. S6). Repulsion of electrons in N<sub>v</sub>-C<sub>3</sub>N<sub>4</sub> by the internal electric field leads to increases on potential energy and upwards on bands bend. Conversely, decreases on potential energy and the downwards on bands bend occur in the C<sub>3</sub>N<sub>4</sub>. Therefore, the photogenerated electrons at the CB of C<sub>3</sub>N<sub>4</sub> are likely to transfer through the interface to recombine with the holes at the VB of N<sub>v</sub>-C<sub>3</sub>N<sub>4</sub>, suggesting a S-scheme charge-transfer process in intra-C<sub>3</sub>N<sub>4</sub> (Fig. 2f) [40].

In the same way, as the work function of N<sub>v</sub>-C<sub>3</sub>N<sub>4</sub> is calculated to be higher than that of C-N<sub>v</sub>-C<sub>3</sub>N<sub>4</sub>, another vertical IEF is created within the VDW carbon nitride homojunction, directing from the top layer of C-N<sub>v</sub>-C<sub>3</sub>N<sub>4</sub> to N<sub>v</sub>-C<sub>3</sub>N<sub>4</sub> (Fig. S7). Combined with the proposed band structures of C-N<sub>v</sub>-C<sub>3</sub>N<sub>4</sub> and N<sub>v</sub>-C<sub>3</sub>N<sub>4</sub>, another S-scheme charge-transfer process is inferred in tandem-C<sub>3</sub>N<sub>4</sub> that photo-excited electrons on the CB of N<sub>v</sub>-C<sub>3</sub>N<sub>4</sub> traverse through the interlayer to the VB of C-N<sub>v</sub>-C<sub>3</sub>N<sub>4</sub> to recombine with the holes, leaving hot electrons on the C-N<sub>v</sub>-C<sub>3</sub>N<sub>4</sub> part (Fig. 2g). On this occasion, the lateral and vertical electrostatic potentials for the three samples were calculated to compare the planar and interlayer energy barriers on charge carriers (Fig. S8). Two layers of the melon sheets were modelled, with a typical VDW distance of 3 Å interlayer separation (Fig. S9). It can be clearly seen that the vertical energy barrier is much higher than the lateral one, meaning that a lateral charge transferring is preferred to a vertical traversing [33]. As such, the photo-excited electrons at the CB of C<sub>3</sub>N<sub>4</sub> prefer to migrate to the VB of N<sub>v</sub>-C<sub>3</sub>N<sub>4</sub> under the lateral IEF, and the hot electrons at the CB of N<sub>v</sub>-C<sub>3</sub>N<sub>4</sub> transfer to the VB of C-N<sub>v</sub>-C<sub>3</sub>N<sub>4</sub> under the vertical IEF (Fig. 2h). As the results, a series of directed IEF is confirmed in the tandem-C<sub>3</sub>N<sub>4</sub>.

The directed IEF in the tandem-C<sub>3</sub>N<sub>4</sub> can be vividly observed by the highest occupied molecular orbital (HOMO) and the lowest unoccupied orbital (LUMO), which provide a pertinent description of the electron orbital configurations at the intralayer contact and interlayer VDW interactions (Fig. 3). The orbitals in both the HOMO and LUMO of benchmark g-C<sub>3</sub>N<sub>4</sub> are symmetric horizontally and vertically. This indicates low intensity of lateral and vertical IEFs in g-C<sub>3</sub>N<sub>4</sub> due to the uniform distribution of electrons. After the construction of intralayer homojunction in intra-C<sub>3</sub>N<sub>4</sub>, the orbitals in both the HOMO and LUMO are non-symmetric within the in-plane. This configuration confirms a lateral IEF in intra-C<sub>3</sub>N<sub>4</sub> due to the non-symmetric concentration of electrons [41]. Further, an interlayer IEF failed to be observed on g-C<sub>3</sub>N<sub>4</sub> and intra-C<sub>3</sub>N<sub>4</sub> because of the similar distribution between the two

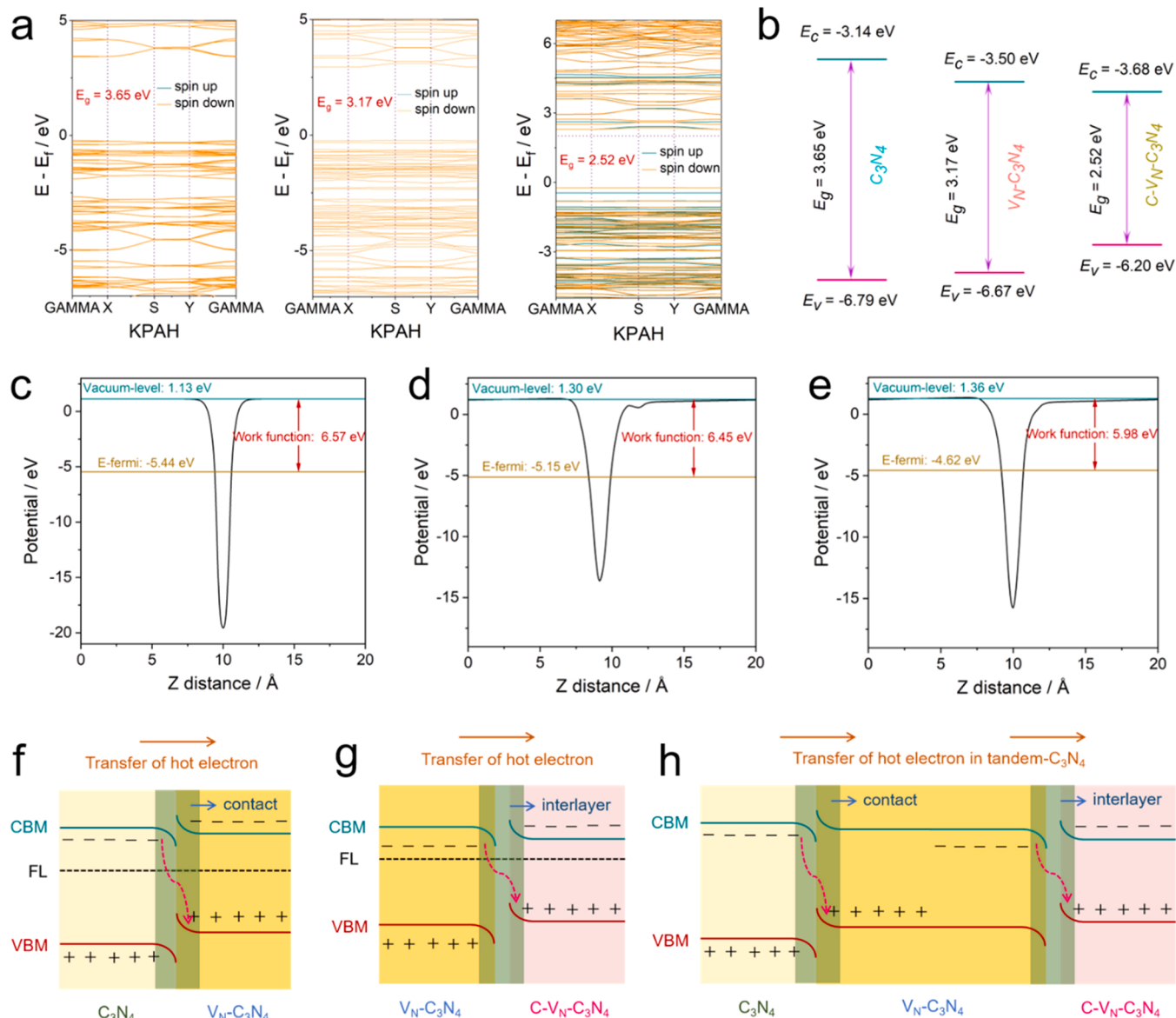


**Fig. 2.** IEF studies in different carbon nitride homojunctions. (a) Calculated bandgap. (b) Band structure. (c-e) Work function for  $\text{C}_3\text{N}_4$ ,  $\text{V}_N\text{-C}_3\text{N}_4$  and  $\text{C-V}_N\text{-C}_3\text{N}_4$ . (f) S-scheme photo-induced electron transfer in intra- $\text{C}_3\text{N}_4$  under light irradiation. (g) S-scheme photo-induced electron transfer in VDW homojunction under light irradiation. (h) A series of directed IEF in tandem- $\text{C}_3\text{N}_4$  with transfer direction of photo-excited hot electron under light irradiation.

layers. For tandem- $\text{C}_3\text{N}_4$ , very interesting details are demonstrated. A same non-symmetric distribution of orbitals as intra- $\text{C}_3\text{N}_4$  is observed within the in-plane. In the meantime, the distributions of orbitals within the bottom layer ( $\text{V}_N\text{-C}_3\text{N}_4$ ) and the top layer ( $\text{C-V}_N\text{-C}_3\text{N}_4$ ) are also totally different. This indicates that a vertical IEF at the VDW junction co-exists with a lateral IEF, proving the series-directed IEF in tandem- $\text{C}_3\text{N}_4$ .

The effect of IEF in intra- $\text{C}_3\text{N}_4$  and tandem- $\text{C}_3\text{N}_4$  on the behaviors of photo-excited charge carriers was then experimentally studied. Steady-state fluorescence spectroscopy is employed to compare the separation rate of photo-excited charge carriers on the prepared samples (PL, Fig. 4a), and a high peak intensity suggests a rapid recombination rate of the charge carriers. As such, compared with g- $\text{C}_3\text{N}_4$ , the separation efficiency of charge carriers after the creation of lateral IEF in intra- $\text{C}_3\text{N}_4$  is dramatically enhanced. However, we cannot see further enhancement on charge separation efficiency after assembling the IEF in tandem- $\text{C}_3\text{N}_4$ . The same trend can be observed from in situ light irradiation electron paramagnetic resonance (EPR) spectra (Fig. 4b) in which the concentration of photoexcited hot electrons can be estimated by the difference of integrated areas of the EPR signals under light irradiation

and in dark (Fig. S10) [42]. The concentrations of  $\text{CB-e}^-$  in intra- $\text{C}_3\text{N}_4$  and tandem- $\text{C}_3\text{N}_4$  are almost the same, and are apparently higher than that of g- $\text{C}_3\text{N}_4$ . These results mean that more hot carriers can be excited driven by lateral IEF forces and the extra vertical electric field in tandem- $\text{C}_3\text{N}_4$  fails to generate more hot carriers.

On this occasion, the movement of hot carriers after their generations toward separations was investigated. First, the lifetimes of hot electrons in intra- $\text{C}_3\text{N}_4$  and tandem- $\text{C}_3\text{N}_4$  were measured (Fig. 4c). Compared with the lifetime of 3.5 ns for intra- $\text{C}_3\text{N}_4$ , the lifetime of hot electrons in tandem- $\text{C}_3\text{N}_4$  turned a bit longer, indicating that the photo-induced hot electrons can move longer, actuated by the series-directed IEF. Besides, the electric impedance of different samples that can affect the movements of hot carriers was tested (Fig. 4d). The impedances of intra- $\text{C}_3\text{N}_4$  and tandem- $\text{C}_3\text{N}_4$  are almost identical, which are much lower than that of g- $\text{C}_3\text{N}_4$ , suggesting the separated hot carriers can be easier to be transported in both homojunctions.

The effect of series-directed IEF in tandem- $\text{C}_3\text{N}_4$  on the transferring orientation of photo-induced charge carriers was also studied. We first used surface photovoltage (SPV) spectra to observe the accumulation

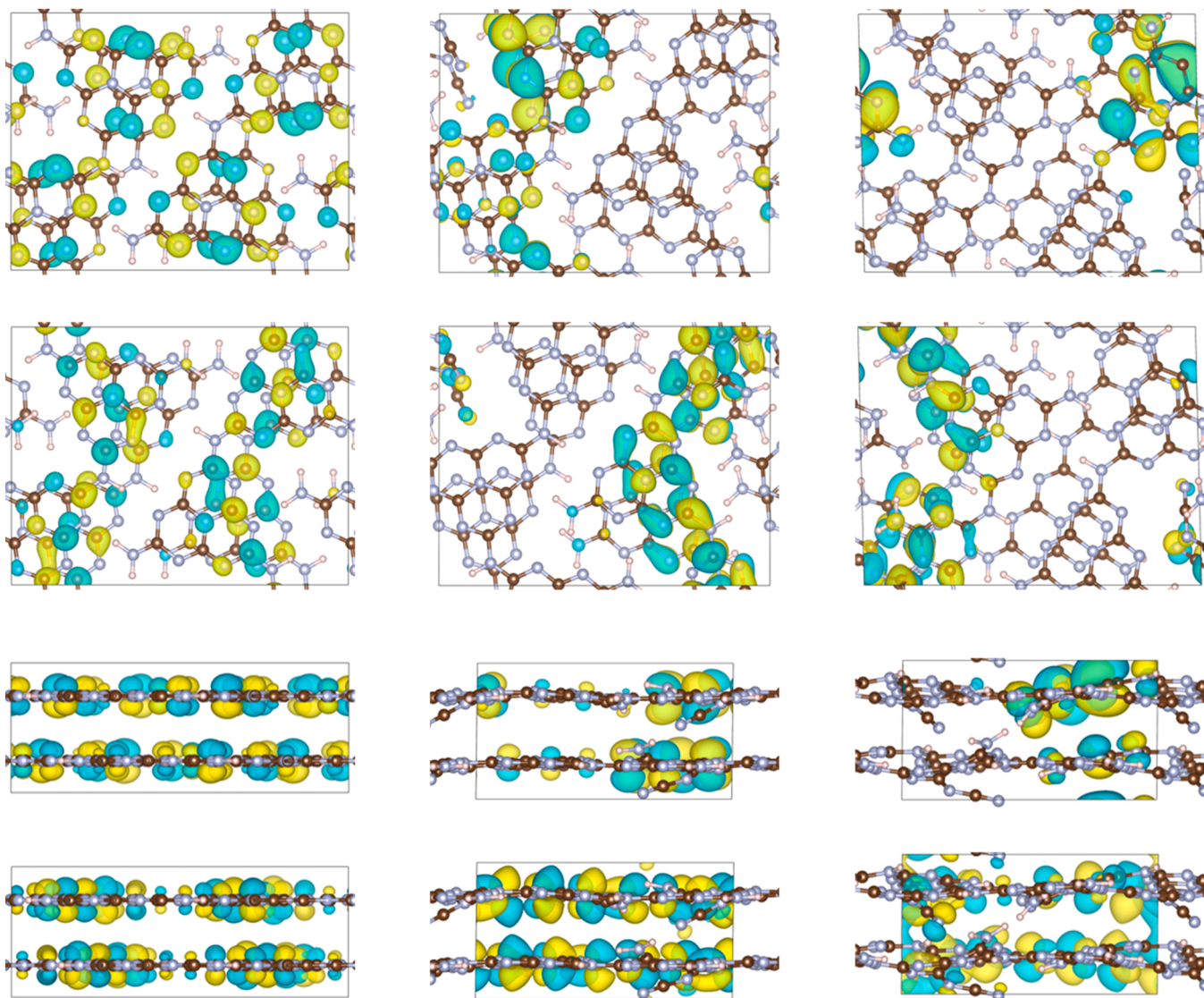


**Fig. 3.** DFT simulations. Front view of HOMO (first line) and LUMO (second line) of g-C<sub>3</sub>N<sub>4</sub> (left), intra-C<sub>3</sub>N<sub>4</sub> (middle) and tandem-C<sub>3</sub>N<sub>4</sub> (right), and side view of HOMO (third line) and LUMO (last line) of g-C<sub>3</sub>N<sub>4</sub> (left), intra-C<sub>3</sub>N<sub>4</sub> (middle) and tandem-C<sub>3</sub>N<sub>4</sub> (right).

region of hot electrons in different samples (Fig. 4e). A weak peak can be found on pristine carbon nitride, confirming the low separation rate of charge carriers in the symmetric and periodic unit cells. After the fabrication of a lateral electric field in intra-C<sub>3</sub>N<sub>4</sub>, the charge dynamics was significantly improved as revealed by the sharp peak in SPV spectra. However, as evidenced by the very positive signal in SPV spectra (Fig. 4e), the activated hot electrons in intra-C<sub>3</sub>N<sub>4</sub> prefer to transfer in the bulk structure rather than to the catalyst surface [43,44]. This is attributed to the negligible vertical IEF in intra-C<sub>3</sub>N<sub>4</sub> and the negative Zeta potential on the surface. After further creation of a vertical IEF between the interlayer of VDW homojunction in tandem-C<sub>3</sub>N<sub>4</sub>, the signal turned much lower. As the charge separation rate after the creation of vertical IEF was barely affected, the weakened peak intensity means that more hot electrons are gathered on the catalyst surface once separated. Furthermore, we also observed the accumulation region of hot electrons by a photo-deposition experiment, where methanol was used as the hole scavenger so that Pt<sup>4+</sup> was reduced to Pt by the photoexcited hot electrons [45]. The TEM images of catalysts after photo-deposition are displayed (Fig. 4f-g). More and larger Pt nanoparticles are deposited on tandem-C<sub>3</sub>N<sub>4</sub> than those on intra-C<sub>3</sub>N<sub>4</sub>, reflecting that the extra vertical IEF in tandem-C<sub>3</sub>N<sub>4</sub> drives more hot electrons to accumulate on the catalyst surface for Pt reduction.

Besides, the abilities of light harvesting and mass transfer after fabrication of lateral and vertical IEFs were studied. g-C<sub>3</sub>N<sub>4</sub> has been revealed to be a visible light responsive photocatalyst (Fig. 5a), however, it is impeded by the weak absorption in the visible light region. After the creation of nitrogen vacancy in intra-C<sub>3</sub>N<sub>4</sub>, the absorption of visible light was improved, with the bandgap narrowed from 2.66 eV for g-C<sub>3</sub>N<sub>4</sub> to 2.62 eV for intra-C<sub>3</sub>N<sub>4</sub> (Fig. S11 and Table S5). A further enhancement is realized on tandem-C<sub>3</sub>N<sub>4</sub> with a long absorption tail extending throughout the whole visible light region. The corresponding bandgap is further decreased to 2.58 eV. The trend in the decreasing bandgap is in a qualitative agreement with the DFT simulation, in which the calculated bandgaps are 3.40, 2.70 and 2.34 eV for g-C<sub>3</sub>N<sub>4</sub>, intra-C<sub>3</sub>N<sub>4</sub> and tandem-C<sub>3</sub>N<sub>4</sub>, respectively (Fig. 5b). From the conduction band determined by Mott-Schottky plots (Fig. S12) and valence band measured by XPS VB spectra (Fig. S13), the band structures of all the three samples were obtained and presented in Fig. S14. The CB and VB positions are gradually dropped down after the fabrication of lateral IEF in intra-C<sub>3</sub>N<sub>4</sub> and further construction of vertical IEF in tandem-C<sub>3</sub>N<sub>4</sub>. The variations from the measurements are consistent with those from DFT calculation, confirming the reliability of both the experimental and simulation results.

The capability of the prepared samples on mass transfer was also

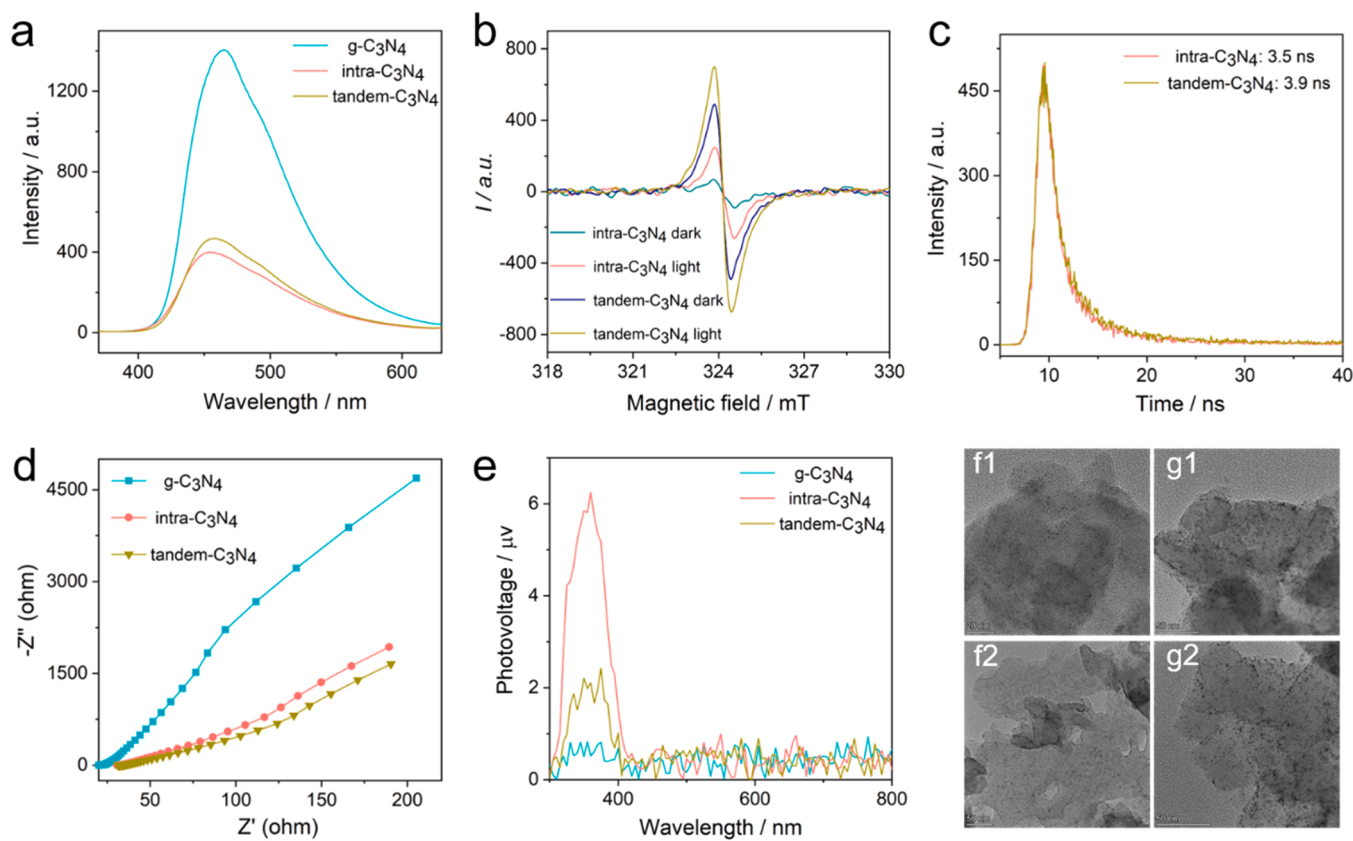


**Fig. 4.** Charge dynamics for different types of carbon nitride photocatalysts. (a) Separation of charge carriers investigated by a steady-state fluorescence spectrometer. (b) Excitation of charge carriers revealed by in situ light irradiation EPR spectra. (c) Lifetime of photoexcited electrons measured by a transient state fluorescence spectrometer. (d) Movement of hot carriers tested by EIS spectra. (e) Direction of movement of hot carriers determined by surface photovoltage spectra. (f-g) Accumulation of photo-excited hot electrons in intra-C<sub>3</sub>N<sub>4</sub> and tandem-C<sub>3</sub>N<sub>4</sub> reflected from the amount and size of photo deposited Pt nanoparticles.

assessed. All the three samples show mesoporous nanostructures, which are proven by the same type of IV isotherm with H<sub>3</sub> hysteresis in the nitrogen adsorption-desorption isotherms (Fig. S15a). The surface areas of intra-C<sub>3</sub>N<sub>4</sub> and tandem-C<sub>3</sub>N<sub>4</sub> samples slightly dropped compared with that of g-C<sub>3</sub>N<sub>4</sub> (Table S5). The pore size distribution of all catalysts is also similar (Fig. S15b). We also measured the contact angles of the prepared samples with water (Fig. 5c). The samples exhibited good hydrophilicity and the contact angles of intra-C<sub>3</sub>N<sub>4</sub> and tandem-C<sub>3</sub>N<sub>4</sub> turned slightly larger than that of g-C<sub>3</sub>N<sub>4</sub>. A larger contact angle would prejudice the mass transfer in photocatalytic water splitting process. Zeta potential of all the prepared samples was collected to clarify the surface charge of homojunctions (Fig. 5d). All of them exhibited negative surface potential, which is beneficial for H<sup>+</sup> adsorption. Compared with g-C<sub>3</sub>N<sub>4</sub>, the surface charge of intra-C<sub>3</sub>N<sub>4</sub> and tandem-C<sub>3</sub>N<sub>4</sub> turned less negative, ascribing to the creations of cyano groups and C=C bonding, respectively.

The photocatalytic performances of these three catalysts were evaluated in water splitting reaction to green hydrogen (Fig. 5e). Pristine g-C<sub>3</sub>N<sub>4</sub> exhibits a low hydrogen evolution rate of 129.5 μmol/h/g, attributing to the weak light absorption and sluggish charge carriers. While a slight improvement on hydrogen evolution rate to 231.5 μmol/h/g was achieved after the formation of intralayer carbon nitride homojunction in intra-C<sub>3</sub>N<sub>4</sub>. A remarkable enhancement on hydrogen production was realized on the integrated three-dimensional homojunction of tandem-C<sub>3</sub>N<sub>4</sub>, with a H<sub>2</sub> production rate of 815 μmol/h/g, which is 6.3 or 3.5 folds higher than those of g-C<sub>3</sub>N<sub>4</sub> and intra-C<sub>3</sub>N<sub>4</sub>, respectively. The performance outperforms reported carbon nitride based photocatalysts (Table S6), indicating the significance of a tandem electric field in tandem-C<sub>3</sub>N<sub>4</sub>. Moreover, the special structure of tandem-C<sub>3</sub>N<sub>4</sub> exhibited an excellent photostability, without an obvious decay in

hydrogen evolution rate after 4 cycles (Fig. S16) [46]. Besides, photocurrent measurements further verified the photocatalytic performance in water splitting reaction (Fig. 5f). Compared with g-C<sub>3</sub>N<sub>4</sub>, a slight and a sharp increase of the photocurrents can be observed on intra-C<sub>3</sub>N<sub>4</sub> and tandem-C<sub>3</sub>N<sub>4</sub>, respectively. The trend is consistent with that of photocatalytic activity, proving the remarkably enhanced photocatalytic activity after assembling the series-directed IEF in tandem-C<sub>3</sub>N<sub>4</sub>.

We summarized the physicochemical, optical and electrochemical properties of the different samples in Table 1 to clarify the contributing factors in intra-C<sub>3</sub>N<sub>4</sub> and tandem-C<sub>3</sub>N<sub>4</sub> to the improved photocatalytic performances. We cannot see much improvements on mass transfer and light harvesting after the fabrication of lateral IEF and tandem IEF in intra-C<sub>3</sub>N<sub>4</sub> and tandem-C<sub>3</sub>N<sub>4</sub>. These two factors on the enhanced photocatalytic hydrogen evolution are thus excluded. Therefore, the enhanced photocatalytic activity in water splitting reaction is attributed to the modification of charge dynamics. Compared with g-C<sub>3</sub>N<sub>4</sub>, it can be clearly inferred that the sharply improved charge dynamics (including separation and mobility) of intra-C<sub>3</sub>N<sub>4</sub> by the lateral driving force contributes to the increased photocatalytic hydrogen evolution rate. However, compared with intra-C<sub>3</sub>N<sub>4</sub>, we fail to see a further enhancement on the separation and movement of charge carriers after the formation of series-directed IEF in tandem-C<sub>3</sub>N<sub>4</sub>. But, more hot electrons can be detected on the surface of tandem-C<sub>3</sub>N<sub>4</sub> under light irradiation. Therefore, it can be concluded that the vertical IEF in the tandem-C<sub>3</sub>N<sub>4</sub> mainly dominates the orientated assembly of photo-generated hot electrons on the surface of the tandem-C<sub>3</sub>N<sub>4</sub>, which is much beneficial for hydrogen production.

To clearly elucidate the contributions of lateral and vertical IEFs in the tandem-C<sub>3</sub>N<sub>4</sub> to the enhanced photocatalytic performances, we calculated the electrostatic potentials and charge density difference to

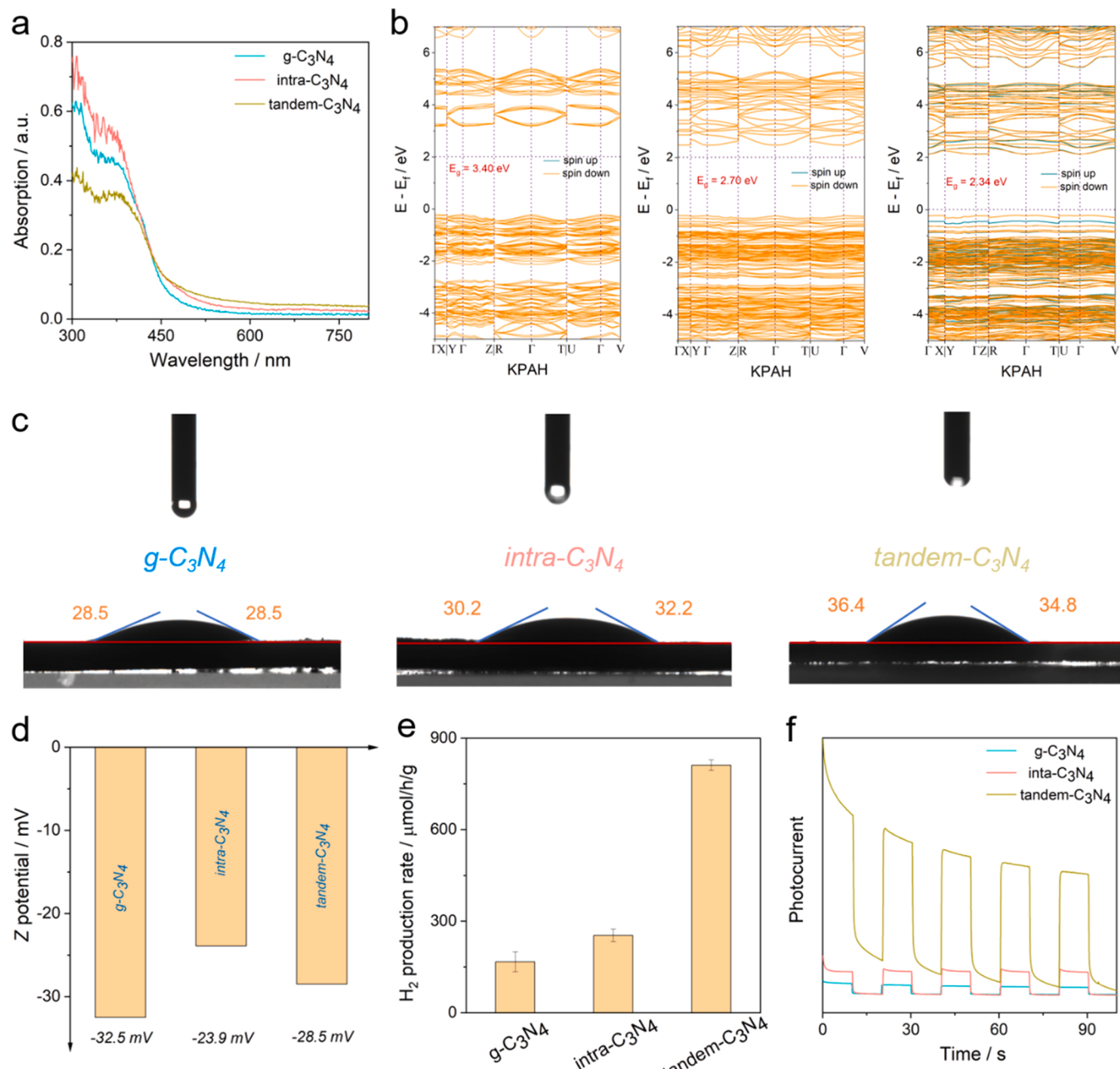


**Fig. 5.** Physicochemical properties and photocatalytic performances of different samples. (a) UV-Vis spectra. (b) Calculated bandgap energies of different samples by DFT simulation. (c) Contact angles. (d) Zeta potentials. (e) Photocatalytic performances in hydrogen evolution from water. (f) Photocurrent tests for different types of carbon nitride homojunction.

**Table 1**

Physicochemical, optical and electrochemical properties of different samples in the three typical processes of photocatalysis.

Sample	Mass transfer		Light harvesting	Charge dynamics			
	Contact angle	BET		UV-Vis	PL	EPR	Lifetime
g-C <sub>3</sub> N <sub>4</sub>	28.6°	8.2 m <sup>2</sup> /g	2.66 eV	high intensity	low		high
intra-C <sub>3</sub> N <sub>4</sub>	31.2°	6.2 m <sup>2</sup> /g	2.62 eV	low intensity	almost the same concentration		low
tandem-C <sub>3</sub> N <sub>4</sub>	35.6°	6.7 m <sup>2</sup> /g	2.56 eV			3.5 ns	3.9 ns

quantify the resistance and IEF force, respectively, on photo-excited hot electrons in the three samples (Fig. 6a-f). The interlayer electrostatic potentials in the three samples are much higher than that within in-plane (Fig. 6g-h). The higher interlayer energy barrier compels photo-induced charge carriers to prefer moving along carbon nitride in-plane

to traversing through the interlayer. As such, in-plane charge transport dominates the overall charge dynamics in carbon nitride materials [33].

For g-C<sub>3</sub>N<sub>4</sub>, the electrostatic potentials within the in-plane and between the interlayer are all maximum, while its lateral and vertical electron transferring amounts are all minimum among the three

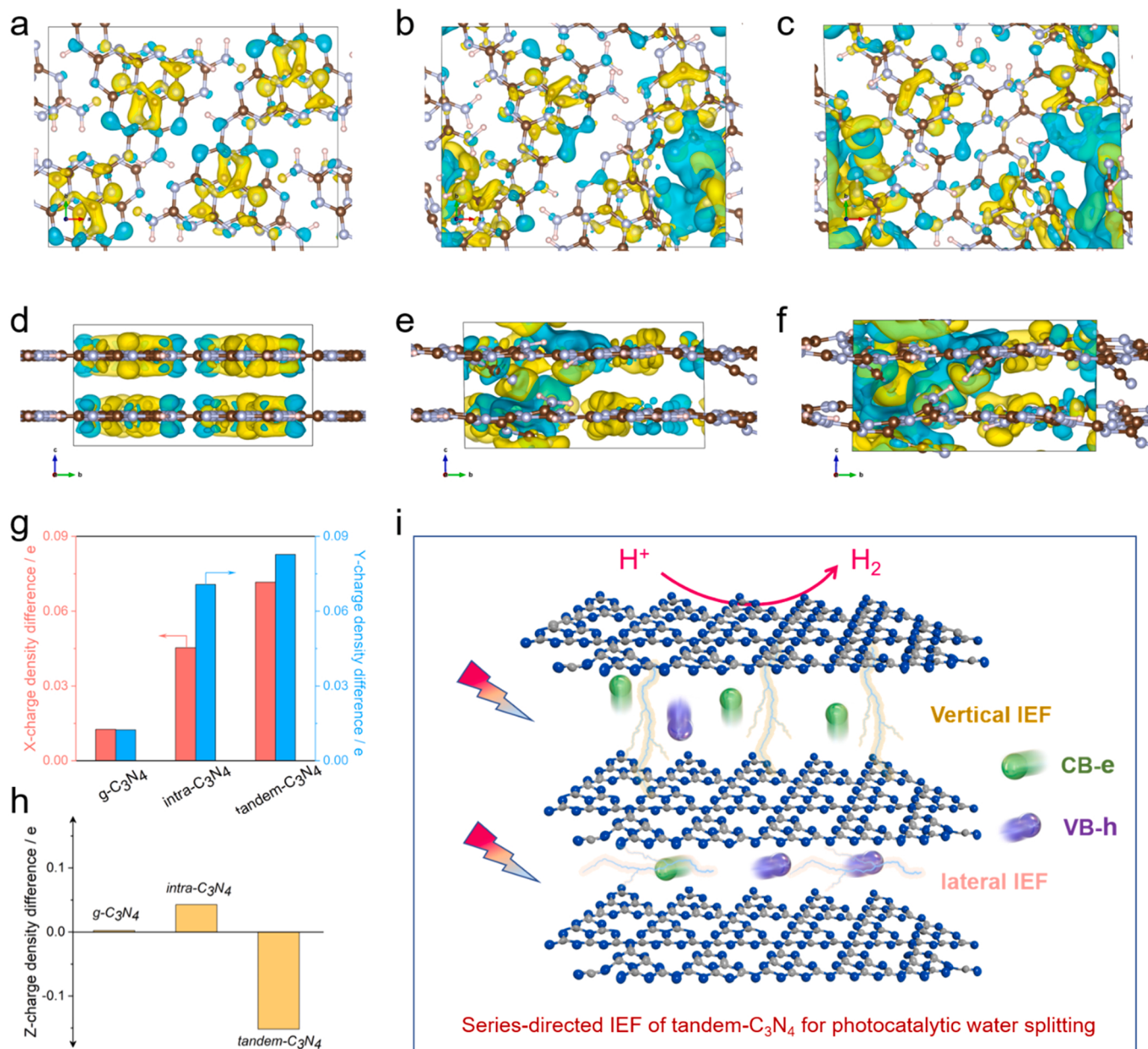


**Fig. 6.** Contributions of lateral and vertical IEF to photocatalysis. Charge density difference for in-plane of (a)  $g\text{-C}_3\text{N}_4$ , (b)  $intra\text{-C}_3\text{N}_4$  and (c)  $tandem\text{-C}_3\text{N}_4$ . Charge density difference for interlayer of (d)  $g\text{-C}_3\text{N}_4$ , (e)  $intra\text{-C}_3\text{N}_4$  and (f)  $tandem\text{-C}_3\text{N}_4$ . Quantitative results are shown in (g) in-plane and (h) interlayer. (i) Reaction mechanism of series-directed IEFs in  $tandem\text{-C}_3\text{N}_4$  for photocatalytic water splitting.

samples. This means that the highest energy barriers and lowest IEF forces among the three samples exist along the in-plane and interlayer of  $g\text{-C}_3\text{N}_4$ . Therefore, the resultant sluggish charge dynamics finally leads to a low photocatalytic hydrogen production rate in  $g\text{-C}_3\text{N}_4$ .

By contrast, the lateral resistance in  $intra\text{-C}_3\text{N}_4$  experiences a significant decrease, and the lateral IEF force is enlarged. As thus, the pockets of charge carriers along the in-plane of  $intra\text{-C}_3\text{N}_4$  are quickly isolated and a dramatic enhancement on the overall charge dynamics is acquired in  $intra\text{-C}_3\text{N}_4$ . In the meantime, the interlayer traversing resistance of  $intra\text{-C}_3\text{N}_4$  decreased and the vertical driving force on hot electrons of  $intra\text{-C}_3\text{N}_4$  increased, indicating that the amount of charge carriers crossing layers is increased. However, the longitudinal movement of hot electrons directs from the surface of  $intra\text{-C}_3\text{N}_4$  to the bulk, resulting in a longer diffusion path for the hot electrons before they involved into hydrogen reduction process [46]. The long diffusion path of hot electrons would easily lead to the decay of the hot electrons and

the very limited enhancement of  $intra\text{-C}_3\text{N}_4$  in photocatalytic hydrogen reduction reaction on the surface [14].

After the fabrication of series-directed IEF in  $tandem\text{-C}_3\text{N}_4$ , the lateral electrostatic potentials and IEF force are not further increased as the structure of lateral homojunction in  $tandem\text{-C}_3\text{N}_4$  is the same as  $intra\text{-C}_3\text{N}_4$ . So, compared with  $intra\text{-C}_3\text{N}_4$ , we cannot see a further enhancement on the charge dynamics in  $tandem\text{-C}_3\text{N}_4$ . Conversely, a smaller vertical electrostatic potential and a larger vertical IEF can be seen after the creation of VDW homojunction on the foundation of  $intra\text{-C}_3\text{N}_4$ . Meanwhile, the vertical IEF in  $tandem\text{-C}_3\text{N}_4$  directs from the top layers to the lower layers. More energetic hot electrons would transfer across a short diffusion pathway (shallow surface layers of  $tandem\text{-C}_3\text{N}_4$ ), accumulate on the surface of  $tandem\text{-C}_3\text{N}_4$  and participate into hydrogen reduction, resulting in a much higher  $\text{H}_2$  production. Therefore,  $tandem\text{-C}_3\text{N}_4$  is integrated by an intralayer homojunction and a VDW homojunction, inducing a lateral IEF and a vertical IEF,

respectively, for a series-directed IEF (Fig. 6i). A lateral IEF contributes to a highly uneven orbital distributions and promotes overall charge dynamics within tandem-C<sub>3</sub>N<sub>4</sub> in plane, while a vertical electric field in the VDW homojunction dominates less on the improvement of charge dynamics but can drive more hot electrons to traverse a short diffusion pathway to the catalyst surface. Compared with the performance enhancement from lateral IEF boosted charge dynamics, a higher surface electron concentration by vertical IEF plays a determining role in the performance enhancement of tandem-C<sub>3</sub>N<sub>4</sub>.

#### 4. Conclusions

We have developed a strategy and employed different techniques to break the intralayer and interlayer symmetries in pristine carbon nitride for integration of a lateral carbon nitride homojunction with a vertical VDW carbon nitride homojunction into a tandem-C<sub>3</sub>N<sub>4</sub>. Theoretical calculations revealed a lateral S-scheme and a vertical S-scheme transfer of photo-excited charge carriers in the intralayer and VDW homojunctions, respectively, realizing a three-dimensional modulation of charge separation and directed movement of photoelectrons. Experiments and DFT calculations collectively confirm that the lateral driving force in intralayer homojunction accelerates the separation and movement of charge carriers, while the additional vertical driving force in VDW homojunction enables more hot electrons to accumulate on the surface of the photocatalyst for reduction reaction. The vertical electric field plays the dominant role in the enhancement of photocatalytic hydrogen production. This work discloses the contributions of lateral and vertical electric fields to photocatalytic activities and blazes a trail to design and synthesize effective photocatalysts for clean hydrogen production and other photocatalytic reactions.

#### CRediT authorship contribution statement

**Jinqiang Zhang:** Conceptualization, Methodology, Data curation, Writing – original draft. **Xiaojie Tan:** Software, Investigation. **Lei Shi:** Data curation. **Haijun Chen:** Resources, Funding acquisition, Supervision. **Yazi Liu:** Conceptualization, Resources. **Shuaijun Wang:** Methodology. **Xiaoguang Duan:** Methodology. **Mingbo Wu:** Resources, Conceptualization. **Hongqi Sun:** Funding acquisition, Data curation, Supervision. **Shaobin Wang:** Project administration, Funding acquisition, Writing – review & editing, Supervision.

#### Declaration of Competing Interest

The authors declare that they have no known competing financial interests or personal relationships that could have appeared to influence the work reported in this paper.

#### Data availability

Data will be made available on request.

#### Acknowledgements

The author (H. Sun) would like to thank the support from ECU Vice-Chancellor's Professorial Research Fellowship. This work is also partially supported by the Australian Research Council (DP170104264 and DP190103548). The support from the National Natural Science Foundation of China (51676096) is acknowledged.

#### Appendix A. Supporting information

Supplementary data associated with this article can be found in the online version at [doi:10.1016/j.apcatb.2023.122781](https://doi.org/10.1016/j.apcatb.2023.122781).

#### References

- [1] J.H. Kim, D. Hansora, P. Sharma, J.W. Jang, J.S. Lee, Toward practical solar hydrogen production - an artificial photosynthetic leaf-to-farm challenge, *Chem. Soc. Rev.* 48 (2019) 1908–1971.
- [2] X. Wang, K. Maeda, A. Thomas, K. Takanabe, G. Xin, J.M. Carlsson, K. Domen, M. Antonietti, A metal-free polymeric photocatalyst for hydrogen production from water under visible light, *Nat. Mater.* 8 (2009) 76–80.
- [3] G. Zhou, Y. Shan, Y. Hu, X. Xu, L. Long, J. Zhang, J. Dai, J. Guo, J. Shen, S. Li, L. Liu, X. Wu, Half-metallic carbon nitride nanosheets with micro grid mode resonance structure for efficient photocatalytic hydrogen evolution, *Nat. Commun.* 9 (2018) 3366.
- [4] S. Yang, Y. Gong, J. Zhang, L. Zhan, L. Ma, Z. Fang, R. Vajtai, X. Wang, P. M. Ajayan, Exfoliated graphitic carbon nitride nanosheets as efficient catalysts for hydrogen evolution under visible light, *Adv. Mater.* 25 (2013) 2452–2456.
- [5] G. Zhang, G. Li, Z.A. Lan, L. Lin, A. Savateev, T. Heil, S. Zafeiratos, X. Wang, M. Antonietti, Optimizing optical absorption, exciton dissociation, and charge transfer of a polymeric carbon nitride with ultrahigh solar hydrogen production activity, *Angew. Chem. Int. Ed.* 56 (2017) 13445–13449.
- [6] J. Zhang, Y. Li, X. Zhao, H. Zhang, L. Wang, H. Chen, S. Wang, X. Xu, L. Shi, L. C. Zhang, J.P. Veder, S. Zhao, G. Nealon, M. Wu, S. Wang, H. Sun, A hydrogen-initiated chemical epitaxial growth strategy for in-plane heterostructured photocatalyst, *ACS Nano* 14 (2020) 17505–17514.
- [7] Akira Fujishima, K. Honda, Electrochemical photolysis of water at a semiconductor electrode, *Nature* 238 (1972) 37–38.
- [8] L. Cheng, Q. Xiang, Y. Liao, H. Zhang, CdS-Based photocatalysts, *Energy Environ. Sci.* 11 (2018) 1362–1391.
- [9] J. Schneider, M. Matsuoka, M. Takeuchi, J. Zhang, Y. Horiuchi, M. Anpo, D. W. Bahnemann, Understanding TiO<sub>2</sub> photocatalysis: mechanisms and materials, *Chem. Rev.* 114 (2014) 9919–9986.
- [10] B. Tian, B. Tian, B. Smith, M.C. Scott, R. Hua, Q. Lei, Y. Tian, Supported black phosphorus nanosheets as hydrogen-evolving photocatalyst achieving 5.4% energy conversion efficiency at 353 K, *Nat. Commun.* 9 (2018) 1397.
- [11] T. Takata, J. Jiang, Y. Sakata, M. Nakabayashi, N. Shibata, V. Nandal, K. Seki, T. Hisatomi, K. Domen, Photocatalytic water splitting with a quantum efficiency of almost unity, *Nature* 581 (2020) 411–414.
- [12] H. Nishiyama, T. Yamada, M. Nakabayashi, Y. Maehara, M. Yamaguchi, Y. Kuromiya, Y. Nagatsuma, H. Tokudome, S. Akiyama, T. Watanabe, R. Narushima, S. Okunaka, N. Shibata, T. Takata, T. Hisatomi, K. Domen, Photocatalytic solar hydrogen production from water on a 100-m<sup>2</sup> scale, *Nature* 598 (2021) 304–307.
- [13] S. Chen, T. Takata, K. Domen, Particulate photocatalysts for overall water splitting, *Nat. Rev. Mater.* 2 (2017) 1–17.
- [14] F. Zhang, Y.-H. Li, M.-Y. Qi, Y.M.A. Yamada, M. Anpo, Z.-R. Tang, Y.-J. Xu, Photothermal catalytic CO<sub>2</sub> reduction over nanomaterials, *Chem. Catal.* 1 (2021) 272–297.
- [15] J. Zhang, L. Wang, X. Zhao, L. Shi, H. Chen, S. Zhang, P. Zhang, S. Wang, L. C. Zhang, Y. Wang, X. Wang, Y. Zhu, H. Zhang, X. Duan, M. Wu, G. Shao, S. Wang, H. Sun, The nature of active sites for plasmon-mediated photothermal catalysis and heat coupled photocatalysis in dry reforming of methane, *Energy Environ. Mater.* (2022), <https://doi.org/10.1002/eem2.12416>.
- [16] J. Zhang, Y. Li, J. Sun, H. Chen, Y. Zhu, X. Zhao, L.-C. Zhang, S. Wang, H. Zhang, X. Duan, L. Shi, S. Zhang, P. Zhang, G. Shao, M. Wu, S. Wang, H. Sun, Regulation of energetic hot carriers on Pt/TiO<sub>2</sub> with thermal energy for photothermal catalysis, *Appl. Catal. B: Environ.* 309 (2022), 121263.
- [17] J. Zhang, X. An, N. Lin, W. Wu, L. Wang, Z. Li, R. Wang, Y. Wang, J. Liu, M. Wu, Engineering monomer structure of carbon nitride for the effective and mild photooxidation reaction, *Carbon* 100 (2016) 450–455.
- [18] S. Wang, J. Zhang, B. Li, H. Sun, S. Wang, Engineered graphitic carbon nitride-based photocatalysts for visible-light-driven water splitting: A review, *Energy Fuels* 35 (2021) 6504–6526.
- [19] H. Zhang, W. Tian, J. Zhang, X. Duan, S. Liu, H. Sun, S. Wang, Carbon nitride-based Z-scheme photocatalysts for non-sacrificial overall water splitting, *Mater. Today Energy* 23 (2022), 100915.
- [20] Y. Li, R. He, P. Han, B. Hou, S. Peng, C. Ouyang, A new concept: Volume photocatalysis for efficient H<sub>2</sub> generation - Using low polymeric carbon nitride as an example, *Appl. Catal. B: Environ.* 279 (2020), 119379.
- [21] Y. Li, M. Ji, Z. Ma, L. Meng, R. He, S. Peng, Hierarchically porous polymeric carbon nitride as a volume photocatalyst for efficient H<sub>2</sub> generation under strong irradiation, *Sol. RRL* 6 (2021) 2100823.
- [22] J. Ran, W. Guo, H. Wang, B. Zhu, J. Yu, S.Z. Qiao, Metal-free 2D/2D phosphorene/g-C<sub>3</sub>N<sub>4</sub> van der Waals heterojunction for highly enhanced visible-light photocatalytic H<sub>2</sub> production, *Adv. Mater.* 30 (2018) 1800128.
- [23] J. Wang, Y. Yu, J. Cui, X. Li, Y. Zhang, C. Wang, X. Yu, J. Ye, Defective g-C<sub>3</sub>N<sub>4</sub>/covalent organic framework van der Waals heterojunction toward highly efficient S-scheme CO<sub>2</sub> photoreduction, *Appl. Catal. B: Environ.* 301 (2022), 120814.
- [24] X. Chen, J. Wang, Y. Chai, Z. Zhang, Y. Zhu, Efficient photocatalytic overall water splitting induced by the giant internal electric field of a g-C<sub>3</sub>N<sub>4</sub>/rGO/PDIP Z-scheme heterojunction, *Adv. Mater.* 33 (2021) 2007479.
- [25] A. Deng, Y. Sun, Z. Gao, S. Yang, Y. Liu, H. He, J. Zhang, S. Liu, H. Sun, S. Wang, Internal electric field in carbon nitride-based heterojunctions for photocatalysis, *Nano Energy* 108 (2023), 108228.
- [26] X. Liu, F. He, Y. Lu, S. Wang, C. Zhao, S. Wang, X. Duan, H. Zhang, X. Zhao, H. Sun, J. Zhang, S. Wang, The double-edged effect of single atom metals on photocatalysis, *Chem. Eng. J.* 453 (2023), 139833.

[27] J. Zhang, Y. Li, X. Zhao, L. Wang, H. Chen, S. Wang, X. Xu, L. Shi, L.-C. Zhang, Y. Zhu, H. Zhang, Y. Liu, G. Nealon, S. Zhang, M. Wu, S. Wang, H. Sun, Aligning potential differences within carbon nitride based photocatalysis for efficient solar energy harvesting, *Nano Energy* 89 (2021), 106357.

[28] Y. Li, P. Han, Y. Hou, S. Peng, X. Kuang, Oriented  $Zn_mIn_2S_{m+3}@In_2S_3$  heterojunction with hierarchical structure for efficient photocatalytic hydrogen evolution, *Appl. Catal. B: Environ.* 244 (2019) 604–611.

[29] Y. Li, Y. Hou, Q. Fu, S. Peng, Y.H. Wu, Oriented growth of  $ZnIn_2S_4/In(OH)_3$  heterojunction by a facile hydrothermal transformation for efficient photocatalytic  $H_2$  production, *Appl. Catal. B: Environ.* 206 (2017) 726–733.

[30] C. Hu, F. Chen, Y. Wang, N. Tian, T. Ma, Y. Zhang, H. Huang, Exceptional cocatalyst-free photo-enhanced piezocatalytic hydrogen evolution of carbon nitride nanosheets from strong in-plane polarization, *Adv. Mater.* 33 (2021) 2101751.

[31] X. Wang, S. Blechert, M. Antonietti, Polymeric graphitic carbon nitride for heterogeneous photocatalysis, *ACS Catal.* 2 (2012) 1596–1606.

[32] W. Wu, J. Zhang, W. Fan, Z. Li, L. Wang, X. Li, Y. Wang, R. Wang, J. Zheng, M. Wu, H. Zeng, Remedy defects in carbon nitride to improve both photooxidation and  $H_2$  generation efficiencies, *ACS Catal.* 6 (2016) 3365–3371.

[33] G. Zhang, J. Zhu, Y. Xu, C. Yang, C. He, P. Zhang, Y. Li, X. Ren, H. Mi, In-plane charge transport dominates the overall charge separation and photocatalytic activity in crystalline carbon nitride, *ACS Catal.* 12 (2022) 4648–4658.

[34] T.Y. Ma, J. Ran, S. Dai, M. Jaroniec, S.Z. Qiao, Phosphorus-doped graphitic carbon nitrides grown *in situ* on carbon-fiber paper: flexible and reversible oxygen electrodes, *Angew. Chem. Int. Ed.* 54 (2015) 4646–4650.

[35] S. Wang, L. Chen, X. Zhao, J. Zhang, Z. Ao, W. Liu, H. Wu, L. Shi, Y. Yin, X. Xu, C. Zhao, X. Duan, S. Wang, H. Sun, Efficient photocatalytic overall water splitting on metal-free 1D SWCNT/2D ultrathin  $C_3N_4$  heterojunctions via novel non-resonant plasmonic effect, *Appl. Catal. B: Environ.* 278 (2020), 119312.

[36] S. Wang, F. He, X. Zhao, J. Zhang, Z. Ao, H. Wu, Y. Yin, L. Shi, X. Xu, C. Zhao, S. Wang, H. Sun, Phosphorous doped carbon nitride nanobelts for photodegradation of emerging contaminants and hydrogen evolution, *Appl. Catal. B: Environ.* 257 (2019), 117931.

[37] H. Yu, R. Shi, Y. Zhao, T. Bian, Y. Zhao, C. Zhou, G.I.N. Waterhouse, L.Z. Wu, C. H. Tung, T. Zhang, Alkali-assisted synthesis of nitrogen deficient graphitic carbon nitride with tunable band structures for efficient visible-light-driven hydrogen evolution, *Adv. Mater.* 29 (2017) 1605148.

[38] Y.-J. Yuan, Z. Shen, S. Wu, Y. Su, L. Pei, Z. Ji, M. Ding, W. Bai, Y. Chen, Z.-T. Yu, Z. Zou, Liquid exfoliation of  $g-C_3N_4$  nanosheets to construct 2D–2D  $MoS_2/g-C_3N_4$  photocatalyst for enhanced photocatalytic  $H_2$  production activity, *Appl. Catal. B: Environ.* 246 (2019) 120–128.

[39] P. Yang, H. Zhuzhang, R. Wang, W. Lin, X. Wang, Carbon vacancies in a melon polymeric matrix promote photocatalytic carbon dioxide conversion, *Angew. Chem. Int. Ed.* 58 (2019) 1134–1137.

[40] D. Zhao, Y. Wang, C.-L. Dong, Y.-C. Huang, J. Chen, F. Xue, S. Shen, L. Guo, Boron-doped nitrogen-deficient carbon nitride-based Z-scheme heterostructures for photocatalytic overall water splitting, *Nat. Energy* 6 (2021) 388–397.

[41] D. Zhao, C.L. Dong, B. Wang, C. Chen, Y.C. Huang, Z. Diao, S. Li, L. Guo, S. Shen, Synergy of dopants and defects in graphitic carbon nitride with exceptionally modulated band structures for efficient photocatalytic oxygen evolution, *Adv. Mater.* (2019) 1903545.

[42] Y. Wang, X. Li, S. Liu, Y. Liu, T. Kong, H. Zhang, X. Duan, C. Chen, S. Wang, Roles of catalyst structure and gas surface reaction in the generation of hydroxyl radicals for photocatalytic oxidation, *ACS Catal.* 12 (2022) 2770–2780.

[43] R. Chen, F. Fan, C. Li, Unraveling charge-separation mechanisms in photocatalyst particles by spatially resolved surface photovoltage techniques, *Angew. Chem. Int. Ed.* 61 (2022) 202117567.

[44] R. Chen, F. Fan, T. Dittrich, C. Li, Imaging photogenerated charge carriers on surfaces and interfaces of photocatalysts with surface photovoltage microscopy, *Chem. Soc. Rev.* 47 (2018) 8238–8262.

[45] Y. Guo, Q. Zhou, J. Nan, W. Shi, F. Cui, Y. Zhu, Perylenetetracarboxylic acid nanosheets with internal electric fields and anisotropic charge migration for photocatalytic hydrogen evolution, *Nat. Commun.* 13 (2022) 2067.

[46] J. Zhang, X. Zhao, L. Chen, S. Li, H. Chen, Y. Zhu, S. Wang, Y. Liu, H. Zhang, X. Duan, M. Wu, S. Wang, H. Sun, Intrinsic mechanisms of morphological engineering and carbon doping for improved photocatalysis of 2D/2D carbon nitride van der Waals heterojunction, *Energy Environ. Mater.* (2022), <https://doi.org/10.1002/eem2.12365>.